

# Magnetic Force Microscopy for Diagnosis of Complex Superconducting Circuits

S.Yu. Grebenschuk<sup>1,2,\*</sup>, R.A. Hovhannisyan,<sup>1</sup> A.G. Shishkin,<sup>1,3</sup> V.V. Dremov<sup>1</sup>, and V.S. Stolyarov<sup>1,3</sup>

<sup>1</sup>Advanced Mesoscience and Nanotechnology Centre, Moscow Institute of Physics and Technology, Dolgoprudny 141700, Russia

<sup>2</sup>Materials Science and Engineering, National University of Singapore, Singapore 117575, Singapore

<sup>3</sup>National University of Science and Technology MISIS, Moscow 119049, Russia



(Received 25 June 2022; revised 12 September 2022; accepted 11 October 2022; published 14 November 2022)

The possibility of controlling Josephson vortices and fluxon states has always been an attractive area of research that can influence the development of superconducting devices and quantum computing. Here we demonstrate the capability of magnetic force microscopy to detect and manipulate Josephson vortices (JVs) and fluxons below the critical current in complex superconducting systems on the example of a dc superconducting quantum interference device. The simultaneous magnetic force microscopy and transport investigation method make it possible to generate JVs by direct current in Josephson junctions and simultaneously analyze their dynamics under various external conditions. Our results show a dynamic process of transition of  $2\pi$ -phase singularities of JVs and fluxons from one to another. Finally, we demonstrated that the magnetic force microscopy method could distinguish the difference in critical currents between several Josephson junctions in complex superconducting circuits without the need of direct electron transport measurements.

DOI: 10.1103/PhysRevApplied.18.054035

## I. INTRODUCTION

The quantum nature of superconductivity gives rise to a multiplicity of macroscopic quantum phenomena. One of the most outstanding of them is the appearance of  $2\pi n$ -phase loops in superconductors.  $2\pi$  singularities in the single connected type-II superconductors are known as Abrikosov vortices (AVs). Methods of detection and manipulation of AVs are well studied by a range of different means, including decoration [1–3], magneto-optics [4,5], scanning tunneling microscopy (STM) [6–8], magnetic force microscopy (MFM) [9,10], superconducting quantum interference device (SQUID) microscopy [11–14], and Lorentz microscopy [15].

The other examples of flux quantization in complex and multiple-connected superconducting systems are Josephson vortices (JVs) and fluxons. While fluxons are well studied by a number of methods, like transport measurements [16,17], Hall micromagnetometry [18,19], scanning Hall probe microscopy [20], SQUID magnetometry [21], scanning SQUID microscopy [22], calorimetry [23], and modified MFM method [24,25], JVs are harder to detect. This is due to their small field gradient and high mobility. However, they have been indirectly studied using the transport measurements (known as Fraunhofer pattern)

or detecting electromagnetic waves by scanning electron microscopy from moving JVs [26,27].

In the past few decades with the rapid development of scanning probe microscopy, MFM proved itself as an effective instrument not only for detection and manipulation of AVs [28], but also for Josephson vortex and fluxon dynamics in superconducting structures [24,25,29,30]. In Ref. [31] it was demonstrated that the MFM method is capable of observing processes in the nondissipation area below the critical current of Fraunhofer pattern and can give more information than usual transport measurements. Moreover, in the same work, it has been shown that a local homogeneous magnetic field can be used for the creation of JVs' ratchetlike movement in a long Josephson junction (JJ). This gives an opportunity for the creation of low dissipation logic for superconducting electronics [32–35].

In this work, we apply simultaneous MFM and transport measurements for studying fluxon dynamics in complex superconducting devices on the example of dc SQUID. While scanning we observe signal responses from AV, JV in the junctions, and fluxons in the ring with a possible transition from JV to fluxon and vice versa. Then, by measuring the dependence of the cantilever frequency on the external field and the value of the current along one of the contacts, we demonstrate peculiar vortex behavior in the sample and the possibility of detecting defects in superconducting devices.

\*sergey.gr.sc@gmail.com

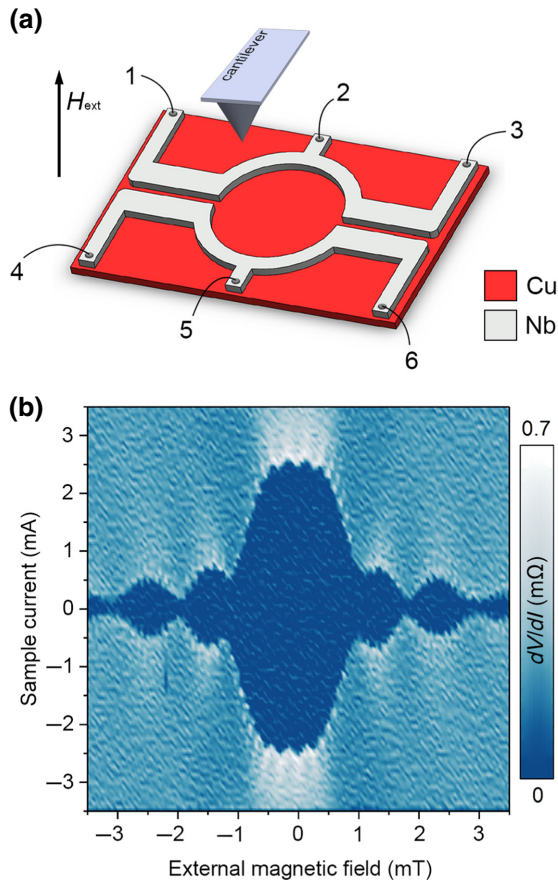


FIG. 1. (a) Scheme of the SQUID with long junctions. The red color is for copper Cu and the light gray color is for niobium Nb. All the six contacts are bonded for the transport measurements; (b)  $I_c(\mu_0 H)$  characteristic of the sample at  $T = 4.2 \text{ K}$ .

Finally, we demonstrate the possibility of analyzing complex systems and distinguishing the difference between Josephson junctions without direct transport measurements and using only the modified MFM technique. Eventually, combining both MFM and transport measurements can be a great tool for the exploration and diagnostic of superconducting electronic devices.

## II. RESULTS AND DISCUSSION

Figure 1(a) shows a sketch of the investigated dc SQUID that consists of Nb superconducting ring with the inner radius  $R_{\text{in}} = 2 \mu\text{m}$  and outer radius  $R_{\text{out}} = 2.5 \mu\text{m}$  and two JJs of SNS type made of Nb/Cu/Nb bilayer. Each junction has a length of  $L \simeq 2.5 \mu\text{m}$  with the width of Cu interlayer of  $t_N = 150 \text{ nm}$  and thickness of  $d_N = 50 \text{ nm}$ . The width of each Nb electrode in the junctions is  $W_{\text{S}1} \simeq W_{\text{S}2} \simeq 1 \mu\text{m}$ , the thickness of Nb electrodes is  $d_S = 100 \text{ nm}$ . The details of sample fabrication could be found in Ref. [29] and in the Appendix.

Figure 1(b) presents the dependence of the basic transport characteristics of the SQUID on an applied magnetic

field at temperature 4.2 K with a cantilever retracted far from the sample to exclude its influence. At this temperature, JJs remain in long state with  $\lambda_J \simeq 350 \text{ nm}$  [29]. The electron transport measurements are carried out in a standard four-terminal configuration using contacts 2–5 for the current setup and 1–4 for voltage measurements [see Fig. 1(a)]. The critical temperature of the superconducting junction in zero applied field is 8.4 K. One can notice that the SQUID has an oscillation period approximately 0.12 mT, which is in a good agreement with the simple estimation  $\mu_0 H_{\text{SQUID}} \simeq \mu_0 (\Phi_0)/(\pi((R_{\text{in}} + R_{\text{out}})/2)^2) \simeq 0.125 \text{ mT}$ , where  $\Phi_0$  is a flux quanta,  $R_{\text{in}}$  and  $R_{\text{out}}$  are the inner and the outer SQUID radii, respectively. The larger oscillation refers to a single JJ and is equal to  $\mu_0 H_{\text{JJ}} \sim 1.1 \text{ mT}$ .

Further, the magnetic probe approached the device and the magnetic properties of the sample are examined at different applied external magnetic fields  $H_{\text{ext}}$  and bias current  $I$  flowing through contacts 1–2.

Figures 2(a)–2(d) show the MFM maps of the sample with  $I = 0 \text{ mA}$  at different applied magnetic fields. As can be seen, in all the scans Nb leads remain in the Meissner state, which creates repulsion of the cantilever and positive shift of tip oscillation frequency (bright areas on the scans). Moreover, one can notice black arcs on both Josephson junctions each of which represents a bifurcation entry (exit) of a JV into (from) the JJ. The way how it happens is as follows: when the probe is close enough, its magnetic field is sufficient to generate or push out a few JVs into the junction. However, when JV enters (exits) the junction, it disrupts the flow of Meissner currents, which eventually results in sudden drops in the probe frequency as screening efficiency is decreased. Such drops in cantilever frequency are seen as arcs in MFM scans. [29,30].

Then, at  $B_{\text{ext}} = -2 \text{ mT}$  [Fig. 2(a)], the magnetic field of the probe is partially compensated, due to which there is only one pair of arcs for each JJ. Then, at 0 mT [Fig. 2(b)] we already see a few pairs of arcs. Interestingly, there is no visible flux in the ring itself even though the field needed for just one flux quanta is almost 10 times less than the one for JJ. It can be explained by the fact that the SQUID ring has a significantly larger inductance than JJ (see the Appendix). As a result, the initial field required for the flux to enter the ring is several times higher than the one for the junctions. Next, in the external magnetic field  $B_{\text{ext}} = 4 \text{ mT}$  [Fig. 2(c)] the flux already entered the loop, as there are concentric rings in the SQUID center in addition to the ones in the junctions. Moreover, the arcs in the junctions are only one sided as they do not have pairs like in (a),(b), which corresponds to the fact that JVs enter (exit) the JJ from one external side and refer to the generation of fluxons in the ring.

At  $-3 \text{ mT}$  [Fig. 2(d)] we see an intermediate case when we have pairs of arcs in JJs and some response from the

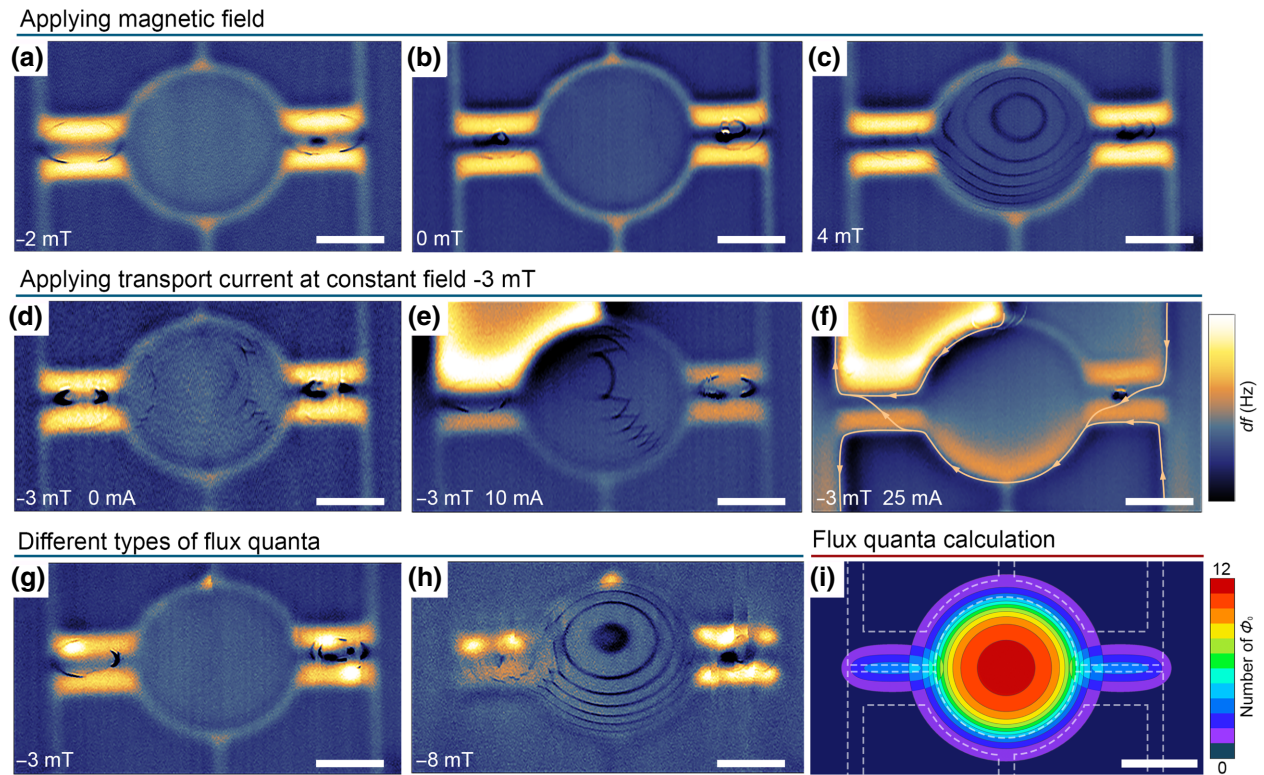


FIG. 2. MFM scans  $6.5 \times 12 \mu\text{m}^2$  at  $T = 4.2 \text{ K}$  of the device at different values of the external magnetic field with zero transport current (a)–(d):  $-2 \text{ mT}$  (a),  $0 \text{ mT}$  (b),  $4 \text{ mT}$  (c), and  $-3 \text{ mT}$  (d). (d)–(f) MFM maps at a certain value of the magnetic field  $= -3 \text{ mT}$  with different current through the contact 1–2:  $I = 0 \text{ mA}$  (d),  $I = 5 \text{ mA}$  (e),  $I = 25 \text{ mA}$  (f). (g),(h) MFM scans with Abrikosov vortices present at  $-3 \text{ mT}$  (g) and  $-8 \text{ mT}$  (h) demonstrate detection of three different types of flux quanta in the same device: Abrikosov vortices, JV, and fluxons in the SQUID. The vertical distance between the MFM probe and the Cu substrate is  $175 \text{ nm}$ . (i) Calculated distribution of the magnetic flux above the sample during scanning at  $H_{ext} = 0 \text{ mT}$ . White dashed contour depicts the sample geometry. The scale bar in all the images corresponds to  $2 \mu\text{m}$ .

fluxons in the SQUID ring. There are also additional transitions between the fluxon states in the ring, which are seen as connections between them. To analyze fluxon states we plot the calculated distribution of flux quanta number across the device at zero external magnetic fields (see the Appendix) during the scanning with MFM cantilever [Fig. 2(i)]. There, we have flux quanta in both JJs and in the SQUID ring, and the boundaries of the states with a different number of flux quanta are very similar to MFM figures. Moreover, in the overlap regions near the junctions, there are similar transitions, which are observed in Fig. 2(d). A distorted image of the rings in the experimental data is related to the slight asymmetry of the magnetic field of the MFM cantilever.

In Figs. 2(e) and 2(f) there is also a transport current that flows through the upper lead of the left junction between contacts 1–2. Magnetic field of the current is well visible in the MFM images as lighter and darker areas around the path of the current flow. In Fig. 2(e) current is  $10 \text{ mA}$ , which is still below the critical value. In that case, arcs in the junction and in the ring are distorted, and as for the ones generated in the SQUID area—they

are not symmetrical due to the inhomogeneous magnetic field of the current from the left side. In this area, there are different sources of the magnetic field: the cantilever magnetic field, the external field from the solenoid, and the generated field from the transport current. The external magnetic field is homogeneous across the scan area, but the contributions of the transport current and cantilever inhomogeneous fields depend on MFM tip position while scanning. While approaching the center of the structure, the influence of the probe increases. From the other side, as we move away from the left upper contact the influence of the transport current decreases. It leads to the asymmetry of the rings and transitions from one ring to another.

In Fig. 2(f) the transport current of  $30 \text{ mA}$  is higher than the critical value and, as the result, the current also starts to flow through the other contacts, which is confirmed too by the picture of lighter and darker areas around the lower part of the device. These darker and lighter shadows can give a clue about the new current path in the system. Since the current generates the magnetic field, the direction of the field is opposite on both sides of the current flow. In the MFM images, the lighter regions correspond to a repulsive

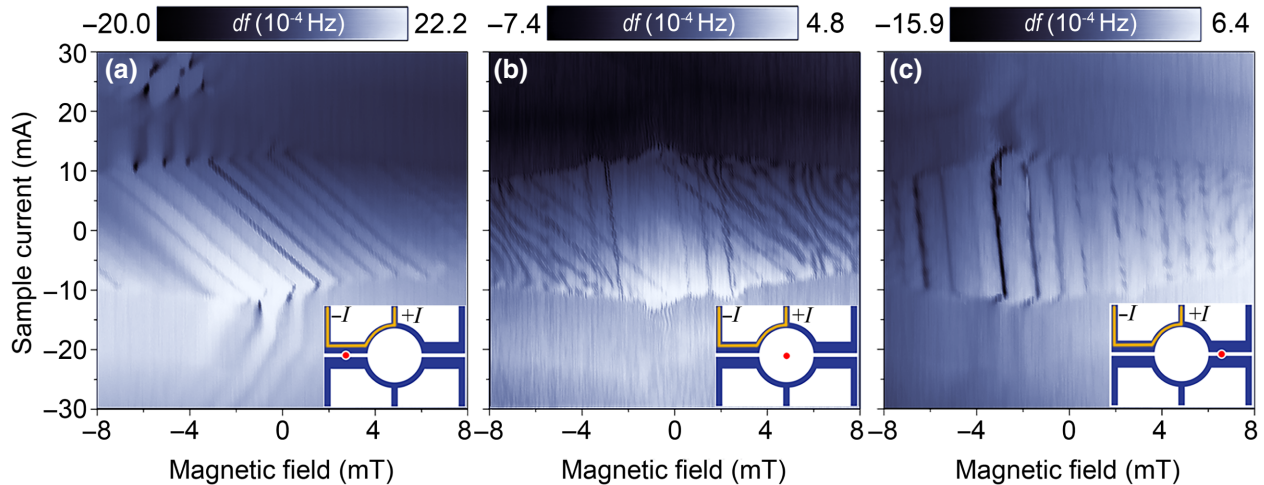


FIG. 3. The frequency shift of the cantilever in dependency on the current along the left junction (contacts 2–1) and external magnetic field at  $T = 4.2$  K for different positions of the tip placed on 150 nm above Cu. (a) Cantilever is above the center of the left junction; (b) in the center of the ring; (c) near the center of the right junction. Insets in each picture show the scheme of the current flow (orange line) in the sample (blue) and the position of the tip (red dot).

force, and the darker ones—to an attractive force. Thus, it is possible to reconstruct the path and the direction of the current flow in the device by following the lighter and the darker regions that appear in the device. It can be seen that when the current values are above critical it flows not only through the upper left contact but also starts to path through the lower part of the ring and contacts 3–6 [the current flow is indicated with arrows in Fig. 2(f)]. The flow of the transport current goes to the other contacts 3–6 as they are connected to each other. Moreover, there are no more dark arcs or rings in the device, which means that fluxons or JVs cannot be detected when the device goes to normal.

Then, after applying a relatively high magnetic field around  $-20$  mT, Abrikosov vortices penetrate into Nb film. During the further decrease of the external magnetic field, some of the vortices remain pinned at lower values of the field, which can be seen as bright spots on Nb leads in Figs. 2(g) and 2(h) for  $-3$  and  $-8$  mT, respectively. Figure 2(g) in contrast to (d) has slightly different arcs in the JJ area and does not have central rings, as Abrikosov vortices in (g) act as sources of inhomogeneous magnetic field and redistribute screening currents in the sample, significantly changing the whole image of the system. At a higher magnetic field, at  $-8$  mT (h), one can see a complex scenario with concentric rings in the central part, bifurcations near the JJ contacts, and Abrikosov vortices in the Nb leads, demonstrating the possibility of the detection of different types of magnetic flux quanta in a single device.

To further study fluxon dynamics in the sample we set up the current flow along only one Josephson junction lead, using contacts 1 and 2. The tip during the measurements is

placed in different positions relative to the device shown by the red dot on the insets of Fig. 3.

The method of Josephson vortex detection in the nondissipating mode proposed in the work [31] gives an opportunity for a deeper analysis of the fluxon dynamics in the superconducting system as a function of the transport current. As the transport current in this experiment flows through the upper right contact 1–2 it creates an additional magnetic field. The results of the observations are presented in Fig. 3. Each abrupt change in frequency of the probe, seen as dark lines, refers to the transition between the states with  $n$  and  $n + 1$  JVs and has the same nature as the arcs in the MFM images in Fig. 2. When the total magnetic field reaches the determined value, the transition between  $n$  and  $n + 1$  states ( $n$  JVs and  $n + 1$  JVs in the junction) occurs. The total magnetic field consists of contributions from the external magnetic field, the magnetic field of the electric current, and the magnetic field generated by the MFM probe. At the big values of the external magnetic field and the transport currents, the lines show almost linear dependency, which corresponds to the total magnetic field in the junction. The field required for the fluxon entrance is the same, thus, the change in the current should be compensated by the external magnetic field. As the current field is  $B \sim I$  according to Biot-Savart law it results in the linear dependencies for the  $I$  and  $B$  values in the case of dips in the cantilever frequency, which correspond to the change from  $n$  to  $n + 1$  (or vice versa) JV state in the system. In our case  $B \sim 26.3(\text{mA})/(\text{mT})I$ . In Fig. 3(a) an average period between the lines at zero electric current is approximately 1.1 mT, which stands for the flux quantization field in the junction.

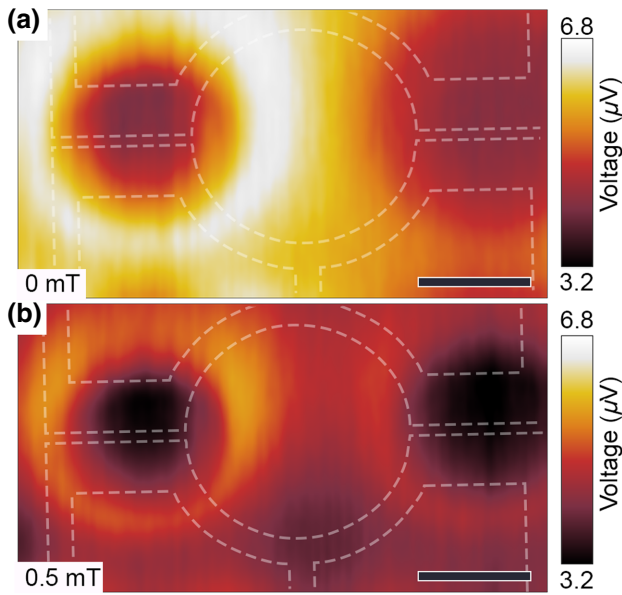


FIG. 4. Maps of the spatial distribution of voltage drop in the device at  $T = 4.2$  K in the external magnetic field: 0 mT (a) and 0.5 mT (b). Dashed white contour shows the actual shape of the sample and its location on the scans. The probe lift height is 175 nm above the substrate. The scale bar corresponds to 2  $\mu\text{m}$ .

Another point worth paying attention to is that on the tilted black lines there is also additional modulation with period  $\Delta B \sim 0.15$  mT (see the Appendix, Fig. 6). It is supposed that this effect corresponds to the interference of the signals from the junction and from the SQUID ring flux quantization, which is approximately 0.12 mT and slightly deviates from the value in the  $I_c(H)$  measurements and estimations.

As for the situation when the magnetic tip is placed above the right JJ, only lines with a bigger tilt are present. The period  $\Delta B \sim 1.1$  mT is almost the same as for the case in (a), which indicates that it is the response from JV in the right JJ. Smaller tilt  $B \sim 2.5(\text{mA})/\text{mT}$  can be explained by the fact that much less magnetic field from the current reaches right JJ, and smaller values of the external magnetic field are needed to compensate for it. If JJ is much further than the current path, the dark lines in the frequency  $df(B, I)$  maps would have turned into vertical ones (along), meaning that JVs, in that case, could only be generated by the external magnetic field. Eventually, such a method is capable of detecting magnetic field gradients from the electrical current itself.

Without changing the transport current configuration, the probe is moved to the center of the SQUID ring [Fig. 3(b)]. It can be noticed that in addition to the existing lines, the lines with a different slope appear with them, and a little further from the center of symmetry, straight lines turn into wavy curves. In the central region in the range from  $-4$  to  $4$  mT two groups of lines with

different tilts are present. The lines with bigger tilt correspond to the entrance (exit) of JVs in the left JJ, as it is closer and more sensitive to the magnetic field of the passing current. The lines with smaller tilt correspond to the right junction, as can be seen from Fig. 3(c). At bigger magnetic fields the lines merge, creating peculiar wavy curves, which mostly consist of two different slopes. Upon sweeping the magnetic field and current, the slope of the curves gradually changes from one to another, and both of these slopes are the same as for individual left and right contacts. It means that at certain conditions JV entered (exited) the circuit through the junction, but at some current and magnetic field values JV started to enter through the other JJ, which resulted in a change of the slope in the curves.

Case in Fig. 3(b) differs from (a) and (c) also by the absence of the signal above the critical current value. The blurred lines above  $I_c$  in (a) and (c) correspond to the further dynamics of the JVs [31]. This behavior is not observable when the probe is in the center of the ring, which can be due to simply pushing out the JVs into the junctions. Moreover, in (a) more features can be seen at even higher current starting from 20 mA at magnetic fields from  $-8$  to  $-4$  mT. Such a high electrical current can create a junction in the ring itself and can occur in the place with light rings in Fig. 2(f), which acts as a phase-slip center. As the result, such a technique also proved itself as a tool for detecting possible defective weak places in the devices due to fabrication.

Next, the voltage maps in dependence on the cantilever position are recorded. To investigate the further influence of the in-homogeneous field of the MFM tip, the sample are scanned by MFM at different applied magnetic fields. Similar to the procedure introduced in Ref. [36], during this process the voltage on the sample is measured as a function of the position of the probe at the defined applied current slightly above the critical value. The voltage is applied between contacts 1 + 3 and 4 + 6 so that the current flow is directly through the weak links of both JJs. To create a bigger difference between the two JJs, the defect is made by the AFM tip on the right junction. As can be noticed, the maps have a circular symmetry, which is related to the symmetry of the field created by the tip. On Fig. 4 voltage maps at fields 0 and 0.5 mT are shown. There, the signal from the junctions is not the same, demonstrating that such a method can possibly distinguish the difference between Josephson junctions even without direct transport measurements. Thus, such a method makes it possible to analyze complex circuits in a noninvasive way, which can incredibly simplify diagnostic of superconducting electronics in the future.

### III. CONCLUSIONS

In conclusion, the developed MFM method allows investigation of the behavior of fluxons in superconducting

structures and analyze their dynamics under different external conditions. Moreover, we assume that while changing the external magnetic field JV in the junctions undergo the transition into fluxon in the superconducting ring and vice versa. Then, measuring the frequency shift of the MFM tip as a function of transport current and external magnetic field while being at a single point above the sample, it is possible to reveal peculiar fluxon dynamics and its transitions in the complex superconducting system and it can also be used as a tool for the defect analysis. Finally, it is shown that the modified MFM method is capable of distinguishing the difference between several JJs without the need for direct transport measurements, which can significantly help in the diagnostics of superconducting electronics.

## ACKNOWLEDGMENTS

We are grateful to V.M. Krasnov for fruitful discussion. Magnetic force microscopy studies are supported by RSF No. 21-72-30026. The sample design and e-beam lithography are supported by the Ministry of Science and Higher Education of the Russian Federation (No. FSMG-2021-0005). Nb film reactive ion etching is supported by the Federal Academic Leadership Program Priority 2030 (NUST MISIS Grant No. K2-2022-029).

## APPENDIX A: METHODS

**Sample fabrication.** Nb/Cu/Nb SNS structures are fabricated using UHV magnetron sputtering, e-beam lithography technique with a hard mask, and reactive ion etching in CF<sub>4</sub> and O<sub>2</sub> atmosphere as follows. First, a Cu film and Nb film are subsequently deposited onto SiO<sub>2</sub>/Si substrate in a single vacuum cycle. The polymer mask for Nb leads is then formed by electron lithography. The pattern is covered by a 20-nm-thick aluminum layer for lift off, and the Al hard mask for Nb leads is formed. Next, the uncovered Nb is etched. After Nb patterning, the Al mask is removed with wet chemistry.

**Magnetic force microscopy.** Magnetic force microscopy measurements are conducted in Attocube Attodry 1000 cryostat equipped with a 9T superconducting magnet, which creates a homogeneous magnetic field in the sample space. For the measurements, we use Bruker-MESP probes with magnetic Co/Cr coating and spring constant  $k = 2.8$  N/m. Before the experiment, the probe is magnetized with a neodymium magnet in the same direction as the magnetic field applied in the cryostat. The MFM scans are performed with a phase-locked loop (PLL) on, and the frequency shift of the cantilever is recorded.

**Transport measurements.** The transport measurements are performed with a standard four-probe configuration. The Fraunhofer pattern was measured in the following approach: for each applied magnetic field, an  $I$ - $V$  curve is measured. The current biased method is

used to measure  $I$ - $V$  curves. The current is swept using Yokogawa GS200 and voltage is measured with Keithley nanovoltmeter 2182.  $dV/dI$  in Fig. 1(b) of the main text is a differential resistance obtained numerically from  $I$ - $V$  curves by a two-point derivative.

## APPENDIX B: FLUX CALCULATION PROCEDURE

To calculate the total flux through the sample we use the so-called point-probe approach. According to this method, stray magnetic fields of the cantilever can be approximated by the magnetic charge  $q$  placed on the distance  $\delta$  from the tip of the probe [36].

Then the magnetic flux created by the cantilever through the SQUID loop and JJs can be found using the relation:

$$\Phi = \frac{q}{4\pi} \Omega, \quad (B1)$$

where  $\Omega$  is the solid angle of the loop and JJ from the perspective of the point charge.

In the case of a loop, this solid angle can be calculated using Eq. (B2)

$$\Omega_{\text{loop}} = \begin{cases} 2\pi + \frac{2H}{L} \left( \frac{r-R}{r+R} \Pi(\alpha^2, k) - K(L) \right), & r < R \\ \frac{2H}{L} \left( \frac{r-R}{r+R} \Pi(\alpha^2, k) - K(L) \right), & r > R, \end{cases} \quad (B2)$$

where  $K, \Pi$  are Legendre's form of the complete elliptic integrals of the first and third order, respectively,  $r$  is a distance of charge projection on the surface of the plane of the loop from its center,  $H = \delta + h$ ,  $L = \sqrt{H^2 + (r+R)^2}$ ,  $k = \sqrt{4rR}/L$ ,  $\alpha = \sqrt{4rR}/(R+r)$ .

For JJ  $\Omega_{\text{JJ}}$  could be found using the equation

$$\Omega_{\text{JJ}} = \sum_{i,j=1}^2 (-1)^{i+j} \operatorname{atan} \left[ \frac{x_i y_j}{H \sqrt{x_i^2 + y_j^2 + H^2}} \right], \quad (B3)$$

where  $\{x_1, x_2, y_1, y_2\}$  are the coordinates of the rectangle with the size  $L \times d + 2\lambda$  (for more details see Ref. [36]).

Finally, to calculate the total flux the parameters  $q = 6.5 \times 10^{-14}$  Wb and  $\delta = 260$  nm are chosen to have the same geometrical properties as the arcs seen in the MFM images. As a result, these parameters turned out to be in good agreement with the actual values shown in Ref. [36].

## APPENDIX C: CALCULATION OF INDUCTANCE

The inductance of SQUID consists of three components

$$L_{\text{SQUID}} = L_K + 2L_{\text{JJ}} + L_G, \quad (C1)$$

where  $L_K$  is a kinetic inductance of the SQUID loop,  $L_G$  is a geometrical inductance of the SQUID loop, and  $L_{\text{JJ}}$  is

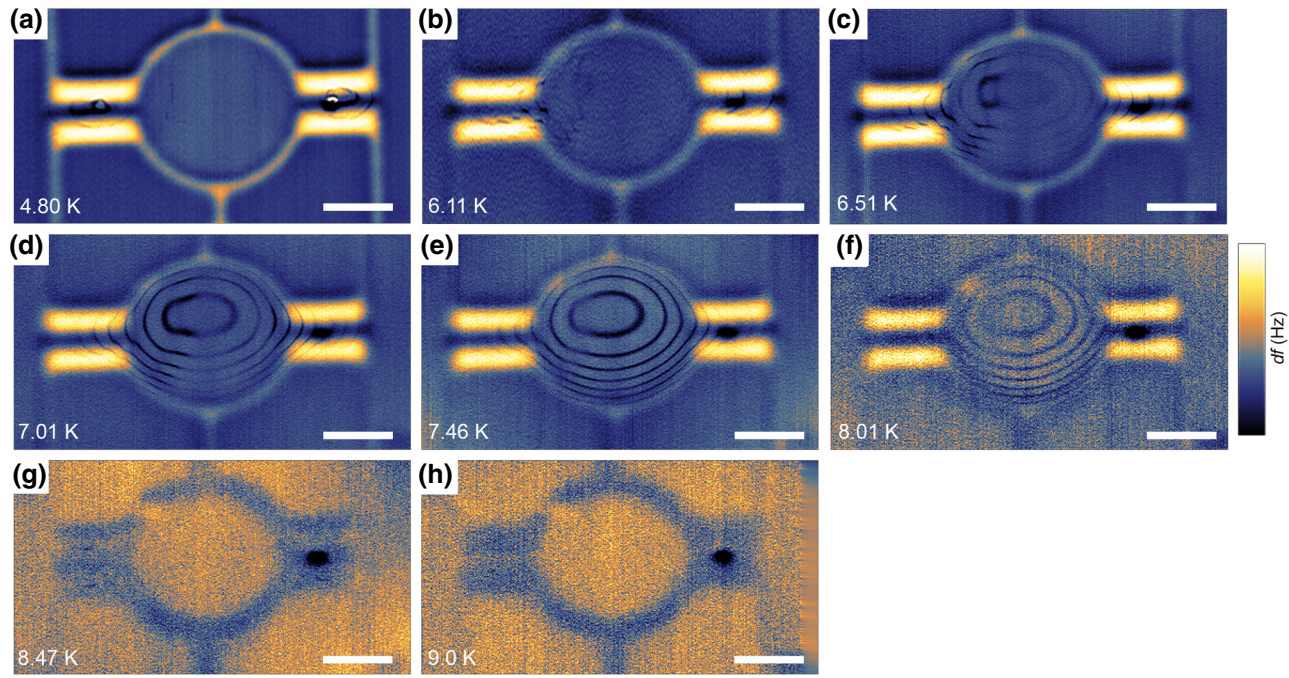


FIG. 5. Temperature dependence of MFM images of the device obtained at zero magnetic field and with no transport current. The distance between the cantilever and the sample is 175 nm. The scale bar corresponds to 2  $\mu\text{m}$ .

an inductance of each JJ. Commonly,  $L_G, L_{\text{JJ}} \gg L_K$ , so the kinetic inductance of the system can be neglected. While the inductance of a single JJ can be approximated easily using the equation  $L_{\text{JJ}} = \Phi_0/2\pi I_c \simeq 2.5 \times 10^{-13} H$ , the calculation of the superconducting loop inductance is more complicated. To determine the term  $L_G$  we approximate the system with five wires with the diameter equal to  $d$  and radius  $R_i = R_{\text{in}} + (i - 1/2)d$  placed concentrically. In this approximation, the total geometrical inductance can be found using the equation

$$L_G \simeq \sum_{i=1}^5 R_i \mu_0 [\ln \frac{4R_i}{d} - 2] = 5.4 \times 10^{-11} H. \quad (\text{C2})$$

Since the inductance  $L_{\text{JJ}} \gg L_G$ , it is more favorable for the system to trap flux quanta in the form of JV rather than as a fluxon in the ring. The situation will change when two energies are equal. To find the total flux that can be carried by JJs before it enters the SQUID we need to solve a simple equation

$$\Phi = \Phi_0 \sqrt{\frac{2L_{\text{JJ}}}{L_G}} \simeq 4\Phi_0. \quad (\text{C3})$$

As can be seen, the calculated value is close to the experimentally observed one.

#### APPENDIX D: MFM TEMPERATURE DEPENDENCE

Figure 5 shows the temperature dependence of MFM scans at zero magnetic field with no transport current through the device. One can notice that the field of the cantilever does not generate flux quanta in the SQUID ring, which remains in the ground state at low temperatures, Fig. 5(a). However, the local inhomogeneous field created by the probe is enough to generate multiple JVs in the weak links. At the elevated temperatures it becomes more favorable for the flux to penetrate directly into the ring, which results in the concentric rings in Figs. 5(b)–5(f). Such a transition is a result of the nonlinear dependence of  $L_{\text{JJ}}$  on the temperature while geometrical inductance of the SQUID  $L_G$  does not depend on the temperature. At temperature  $T = 6.1$  K, an intermediate state can be observed when the geometrical inductance is equal to  $2L_{\text{JJ}}$ . At higher temperatures  $L_{\text{JJ}}$  becomes larger than the geometrical inductance and black rings can be already observed.

At temperatures close to the critical and higher, the sample undergoes a transition from the superconducting to the normal state [Figs. 5(g) and 5(h)]. At these temperatures, there is no Meissner state and only the influence of the sample topography is seen. An additional weak spot in the upper left part becomes visible in the normal state. As in the normal state there is no screening, there is also no repulsive force acting on the probe, and we see only the larger attractive force from the surface spots that are closer

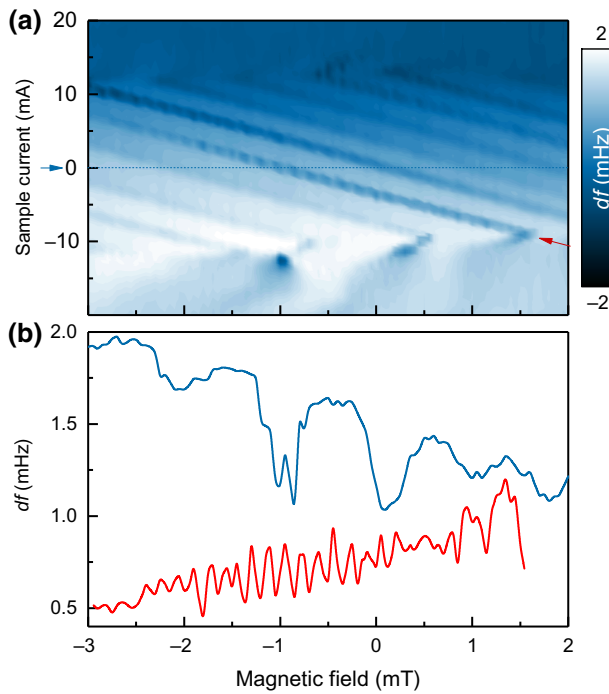


FIG. 6. (a) Frequency shift of the cantilever dependency on the current along the left junction (contacts 2–1) and the external magnetic field for the case when the tip is placed 150 nm above the center of the left junction. The figure is an enlargement of Fig. 3(a) of the main text. (b) Cross sections of (a). The blue curve stands for a cross section of (a) at zero current (indicated with a dashed line in (a), and the red curve is a cross section along the diagonal line indicated with the red arrow in (a). The cross sections are shifted along  $df$  ( $Y$  axis) for better visibility.

to the tip, so it should correlate with the sample geometry. The weak spot means that there is a constriction in the device, which appears during the fabrication process. Besides, one can notice a black dot in the center of the right JJ. As stated in the main text, such a defect is created with an AFM probe to introduce additional slight asymmetry in the system to show capabilities of MFM to detect difference in the similar JJs.

#### APPENDIX E: FLUX QUANTIZATION IN THE SQUID IN THE $df(B, I)$ DEPENDENCY

It is demonstrated in the MFM images in Fig. 2 that both the arcs (from JVs) in JJ and the rings (fluxons) in the SQUID can be seen simultaneously. It means that while performing  $df(B, I)$  measurements introduced in Fig. 3 it should also be possible to detect both JVs in the nearest junction and fluxons in the rings. Figure 6(a) shows an enlarged region of Fig. 3(a) from the main text, when the tip is placed above the center of the left junction and the current flows through the left upper lead of the left JJ between contacts 1 and 2. It is already shown in the main text that the black lines with periodicity 1.1 mT correspond

to the entrance (exit) of the JV in the left JJ. However, one can also notice additional modulation with a smaller period along some of the black lines. Figure 6(b) shows cross sections at zero current (blue) and along one of the tilted lines [red, indicated with red arrow in (a)]. The periodicity of the red curve corresponds to  $\Delta B \sim 0.15$  mT, which is quite close to the value 0.12 mT obtained from the  $I_c(B)$  measurements and from the estimations for the SQUID ring. From this, we can suggest that this modulation comes from the fluxons in the SQUID itself.

- [1] C. Bolle, P. Gammel, D. Grier, C. Murray, D. Bishop, D. Mitzi, and A. Kapitulnik, Observation of a Commensurate Array of Flux Chains in Tilted Flux Lattices in Bi-Sr-Ca-Cu-O Single Crystals, *Phys. Rev. Lett.* **66**, 112 (1991).
- [2] A. Bezryadin, Y. N. Ovchinnikov, and B. Pannetier, Nucleation of vortices inside open and blind microholes, *Phys. Rev. B* **53**, 8553 (1996).
- [3] I. Grigorieva, W. Escoffier, J. Richardson, L. Vinnikov, S. Dubonos, and V. Oboznov, Direct Observation of Vortex Shells and Magic Numbers in Mesoscopic Superconducting Disks, *Phys. Rev. Lett.* **96**, 077005 (2006).
- [4] P. Goa, H. Hauglin, Å. A. Olsen, M. Baziljevich, and T. Johansen, Magneto-optical imaging setup for single vortex observation, *Rev. Sci. Instrum.* **74**, 141 (2003).
- [5] I. S. Veshchunov, W. Magrini, S. Mironov, A. Godin, J.-B. Trebbia, A. I. Buzdin, P. Tamarat, and B. Lounis, Optical manipulation of single flux quanta, *Nat. Commun.* **7**, 1 (2016).
- [6] H. Suderow, I. Guillamón, J. G. Rodrigo, and S. Vieira, Imaging superconducting vortex cores and lattices with a scanning tunneling microscope, *Supercond. Sci. Technol.* **27**, 063001 (2014).
- [7] G. C. Ménard, S. Guissart, C. Brun, S. Pons, V. S. Stolyarov, F. Debontridder, M. V. Leclerc, E. Janod, L. Cario, D. Roditchev, Pascal Simon, and Tristan Cren, Coherent long-range magnetic bound states in a superconductor, *Nat. Phys.* **11**, 1013 (2015).
- [8] A. Hasnat, Static properties of superconducting pyramidal STM tip in the presence of a vortex, *Physica C: Supercond. Appl.* **593**, 1354011 (2022).
- [9] A. Correa, F. Mompeán, I. Guillamón, E. Herrera, M. García-Hernández, T. Yamamoto, T. Kashiwagi, K. Kadouaki, A. I. Buzdin, H. Suderow, and Carmen Munuera, Attractive interaction between superconducting vortices in tilted magnetic fields, *Commun. Phys.* **2**, 1 (2019).
- [10] J. B. Llorens, L. Embon, A. Correa, J. D. González, E. Herrera, I. Guillamón, R. F. Luccas, J. Azpeitia, F. J. Mompeán, M. García-Hernández, Carmen Munuera, Jazmín Aragón Sánchez, Yanina Fasano, Milorad V. Milošević, Hermann Suderow, and Yonathan Anahory, Observation of a gel of quantum vortices in a superconductor at very low magnetic fields, *Phys. Rev. Res.* **2**, 013329 (2020).
- [11] J. Kirtley, C. Tsuei, M. Rupp, J. Sun, L. S. Yu-Jahnes, A. Gupta, M. Ketchen, K. Moler, and M. Bhushan, Direct Imaging of Integer and Half-Integer Josephson Vortices in High- $T_c$  Grain Boundaries, *Phys. Rev. Lett.* **76**, 1336 (1996).

- [12] H. Hilgenkamp, H.-J. H. Smilde, D. H. Blank, G. Rijnders, H. Rogalla, J. R. Kirtley, and C. C. Tsuei, Ordering and manipulation of the magnetic moments in large-scale superconducting  $\pi$ -loop arrays, *Nature* **422**, 50 (2003).
- [13] D. Vasyukov, Y. Anahory, L. Embo, D. Halbertal, J. Cuppens, L. Neeman, A. Finkler, Y. Segev, Y. Myasoedov, M. L. Rappaport, Martin E. Huber, and Eli Zeldov, A scanning superconducting quantum interference device with single electron spin sensitivity, *Nat. Nanotechnol.* **8**, 639 (2013).
- [14] L. Embo, Y. Anahory, Ž. L. Jelić, E. O. Lachman, Y. Myasoedov, M. E. Huber, G. P. Mikitik, A. V. Silhanek, M. V. Milošević, A. Gurevich, and E. Zeldov, Imaging of superfast dynamics and flow instabilities of superconducting vortices, *Nat. Commun.* **8**, 1 (2017).
- [15] T. Matsuda, K. Harada, H. Kasai, O. Kamimura, and A. Tonomura, Observation of dynamic interaction of vortices with pinning centers by lorentz microscopy, *Science* **271**, 1393 (1996).
- [16] R. Parks, and W. Little, Fluxoid quantization in a multiply-connected superconductor, *Phys. Rev.* **133**, A97 (1964).
- [17] M. Morelle, D. S. Golubović, and V. V. Moshchalkov, Nucleation of superconductivity in a mesoscopic loop of varying width, *Phys. Rev. B* **70**, 144528 (2004).
- [18] S. Pedersen, G. Kofod, J. Hollingbery, C. Sørensen, and P. Lindelof, Dilation of the giant vortex state in a mesoscopic superconducting loop, *Phys. Rev. B* **64**, 104522 (2001).
- [19] D. Y. Vodolazov, F. Peeters, S. Dubonos, and A. Geim, Multiple flux jumps and irreversible behavior of thin Al superconducting rings, *Phys. Rev. B* **67**, 054506 (2003).
- [20] D. Davidović, S. Kumar, D. H. Reich, J. Siegel, S. Field, R. Tiberio, R. Hey, and K. Ploog, Correlations and Disorder in Arrays of Magnetically Coupled Superconducting Rings, *Phys. Rev. Lett.* **76**, 815 (1996).
- [21] X. Zhang and J. C. Price, Susceptibility of a mesoscopic superconducting ring, *Phys. Rev. B* **55**, 3128 (1997).
- [22] J. Kirtley, C. Tsuei, V. Kogan, J. Clem, H. Raffy, and Z. Li, Fluxoid dynamics in superconducting thin film rings, *Phys. Rev. B* **68**, 214505 (2003).
- [23] O. Bourgeois, S. Skipetrov, F. Ong, and J. Chaussy, Attojoule Calorimetry of Mesoscopic Superconducting Loops, *Phys. Rev. Lett.* **94**, 057007 (2005).
- [24] H. Polshyn, T. R. Naibert, and R. Budakian, Imaging phase slip dynamics in micron-size superconducting rings, *Phys. Rev. B* **97**, 184501 (2018).
- [25] H. Polshyn, T. Naibert, and R. Budakian, Manipulating multivortex states in superconducting structures, *Nano Lett.* **19**, 5476 (2019).
- [26] A. Laub, T. Doderer, S. Lachenmann, R. Huebener, and V. Oboznov, Lorentz Contraction of Flux Quanta Observed in Experiments with Annular Josephson Tunnel Junctions, *Phys. Rev. Lett.* **75**, 1372 (1995).
- [27] V. M. Krasnov, Josephson junctions in a local inhomogeneous magnetic field, *Phys. Rev. B* **101**, 144507 (2020).
- [28] O. M. Auslaender, L. Luan, E. W. Straver, J. E. Hoffman, N. C. Koshnick, E. Zeldov, D. A. Bonn, R. Liang, W. N. Hardy, and K. A. Moler, Mechanics of individual isolated vortices in a cuprate superconductor, *Nat. Phys.* **5**, 35 (2009).
- [29] V. V. Dremov, S. Y. Grebenchuk, A. G. Shishkin, D. S. Baranov, R. A. Hovhannisan, O. V. Skryabina, N. Lebedev, I. A. Golovchanskiy, V. I. Chichkov, C. Brun, Tristan Cren, Vladimir M. Krasnov, Alexander A. Golubov, Dimitri Roditchev, and Vasily S. Stolyarov, Local Josephson vortex generation and manipulation with a magnetic force microscope, *Nat. Commun.* **10**, 1 (2019).
- [30] S. Y. Grebenchuk, R. A. Hovhannisan, V. V. Dremov, A. G. Shishkin, V. I. Chichkov, A. A. Golubov, D. Roditchev, V. M. Krasnov, and V. S. Stolyarov, Observation of interacting Josephson vortex chains by magnetic force microscopy, *Phys. Rev. Res.* **2**, 023105 (2020).
- [31] V. S. Stolyarov, V. Ruzhitskiy, R. A. Hovhannisan, S. Grebenchuk, A. G. Shishkin, O. V. Skryabina, I. A. Golovchanskiy, A. A. Golubov, N. V. Klenov, I. I. Soloviev, Mikhail Yu. Kupriyanov, Alexander Andriyash, and Dimitri Roditchev, Revealing Josephson vortex dynamics in proximity junctions below critical current, *Nano Lett.* **22**, 5715 (2022).
- [32] C.-S. Lee, B. Janko, I. Derenyi, and A.-L. Barabási, Reducing vortex density in superconductors using the ‘ratchet effect’, *Nature* **400**, 337 (1999).
- [33] J. Villegas, S. Savel’ev, F. Nori, E. Gonzalez, J. Anguita, R. Garcia, and J. Vicent, A superconducting reversible rectifier that controls the motion of magnetic flux quanta, *Science* **302**, 1188 (2003).
- [34] B. Zhu, F. Marchesoni, V. Moshchalkov, and F. Nori, Controllable step motors and rectifiers of magnetic flux quanta using periodic arrays of asymmetric pinning defects, *Phys. Rev. B* **68**, 014514 (2003).
- [35] C. C. de Souza Silva, J. Van de Vondel, M. Morelle, and V. V. Moshchalkov, Controlled multiple reversals of a ratchet effect, *Nature* **440**, 651 (2006).
- [36] R. A. Hovhannisan, S. Y. Grebenchuk, D. S. Baranov, D. Roditchev, and V. S. Stolyarov, Lateral josephson junctions as sensors for magnetic microscopy at nanoscale, *J. Phys. Chem. Lett.* **12**, 12196 (2021).